

## Enhancement of Mesoscale Eddy Stirring at Steering Levels in the Southern Ocean

RYAN ABERNATHEY, JOHN MARSHALL, AND MATT MAZLOFF

*Department of Earth, Atmospheric and Planetary Sciences, Massachusetts Institute of Technology, Cambridge, Massachusetts*

EMILY SHUCKBURGH

*British Antarctic Survey, Cambridge, United Kingdom*

(Manuscript received 17 December 2008, in final form 26 June 2009)

### ABSTRACT

Meridional cross sections of effective diffusivity in the Southern Ocean are presented and discussed. The effective diffusivity,  $K_{\text{eff}}$ , characterizes the rate at which mesoscale eddies stir properties on interior isopycnal surfaces and laterally at the sea surface. The distributions are obtained by monitoring the rate at which eddies stir an idealized tracer whose initial distribution varies monotonically across the Antarctic Circumpolar Current (ACC). In the absence of observed maps of eddying currents in the interior ocean, the advecting velocity field is taken from an eddy-permitting state estimate of the Southern Ocean (SOSE). A three-dimensional advection–diffusion equation is solved and the diffusivity diagnosed by applying the Nakamura technique on both horizontal and isopycnal surfaces. The resulting meridional sections of  $K_{\text{eff}}$  reveal intensified isopycnal eddy stirring (reaching values of  $\sim 2000 \text{ m}^2 \text{ s}^{-1}$ ) in a layer deep beneath the ACC but rising toward the surface on the equatorward flank. Lower effective diffusivity values ( $\sim 500 \text{ m}^2 \text{ s}^{-1}$ ) are found near the surface where the mean flow of the ACC is strongest. It is argued that  $K_{\text{eff}}$  is enhanced in the vicinity of the steering level of baroclinic waves, which is deep along the axis of the ACC but shallows on the equatorial flank. Values of  $K_{\text{eff}}$  are also found to be spatially correlated with gradients of potential vorticity on isopycnal surfaces and are large where those gradients are weak and vice versa, as expected from simple dynamical arguments. Finally, implications of the spatial distributions of  $K_{\text{eff}}$  for the dynamics of the ACC and its overturning circulation are discussed.

### 1. Introduction

The Southern Ocean is a place of both strong eddy activity and strong mean flows. One might expect vigorous eddies to be efficient at mixing tracers. However, strong jets can inhibit transport across their axes. In fact, spatially inhomogeneous mixing and the jet-formation mechanism appear to be fundamentally linked through potential vorticity (PV) dynamics (Haynes et al. 2007; Dritschel and McIntyre 2008). Furthermore, baroclinic currents can have different transport properties at different vertical levels. These vertical variations in eddy mixing in the troposphere and stratosphere have been investigated by Haynes and Shuckburgh (2000a,b), and

also recently in more idealized models of baroclinic jets by, for instance, Greenslade and Haynes (2008; see also Esler 2008a,b). In an ocean context, Bower et al. (1985) suggested the Gulf Stream acts as a transport barrier near the surface but mixes strongly across the front at depth. This observation was followed by numerous Lagrangian studies that confirmed the general picture (Bower and Rossby 1989; Bower 1991; Rogerson et al. 1999; Yuan et al. 2002). Here we investigate the meridional and vertical variations of mesoscale eddy mixing in the Southern Ocean using a tracer-based approach.

Our work builds on the paper of Marshall et al. (2006, hereafter MSJH), who drove an advection–diffusion model with surface velocities computed from satellite altimetry. In their study, an initial tracer distribution with a prescribed monotonic gradient across the Antarctic Circumpolar Current (ACC) was stirred and mixed by the two-dimensional eddying flow. The theoretical framework set out by Nakamura (1996) was then applied to the tracer distribution. The resulting “effective diffusivity,”

*Corresponding author address:* Ryan Abernathey, Department of Earth, Atmospheric and Planetary Sciences, Massachusetts Institute of Technology, Room 54-1421, 77 Massachusetts Avenue, Cambridge, MA 02139.  
E-mail: rpa@mit.edu

$K_{\text{eff}}$ , characterizes the rate of mixing by eddies acting laterally at the sea surface. An interesting meridional structure emerged, with enhanced mixing rates ( $\sim 2000 \text{ m}^2 \text{ s}^{-1}$ ) on the equatorial flank and evidence of suppressed mixing ( $\sim 500 \text{ m}^2 \text{ s}^{-1}$ ) near the core of the ACC. This result was consistent with the notion that the mean flow was acting to suppress mixing.

Smith and Marshall (2009, hereafter SM), echoing earlier work by Treguier (1999), suggested that although  $K_{\text{eff}}$  is small in the core of the ACC at the sea surface, it might be expected to be enhanced near the steering level of baroclinic waves growing on the thermal wind shear of the ACC. Employing a linear quasigeostrophic stability analysis of a hydrographic climatology of the Southern Ocean, SM showed that the steering level of the fastest-growing unstable modes resides at a depth of order 1.5 km and is roughly coincident with the level at which the meridional quasigeostrophic potential vorticity (QGPV) gradient changes sign. Linear theory (Green 1970; Marshall 1981; Killworth 1997) suggests that the eddy diffusivity of a growing baroclinic wave has a maximum at the steering level. Moreover, in calculations with a nonlinear stacked QG model, SM confirmed that this linear result survives in the nonlinear regime. They also presented observational evidence that the phase of surface altimetric signals, the surface signature of interior baroclinic instability, propagates downstream at roughly  $2 \text{ cm s}^{-1}$ , the speed of the mean current at a depth of 1.5 km or so, and much slower than the  $10 \text{ cm s}^{-1}$  mean surface current.

Here our goal is to map the meridional *and depth* structure of  $K_{\text{eff}}$  in the Southern Ocean using the effective diffusivity methodology set out by Nakamura (1996). In the absence of observed three-dimensional velocity fields, we make use of an eddying numerical state estimate of the Southern Ocean tightly constrained by observations, and we diagnose  $K_{\text{eff}}$  from the tracer distribution on isopycnal surfaces. The resulting effective diffusivity cross sections support the notion of intensified mixing at depth and also reveal that deep mixing below the ACC connects with the heightened surface mixing found by MSJH on the equatorward flank. The structure of  $K_{\text{eff}}$  contains the signature of a critical layer, wherein the interplay between upstream-propagating waves and eastward mean flow determines where mixing is enhanced and suppressed.

Our paper is organized in the following way: section 2 contains a description of the state estimate and the machinery used to calculate effective diffusivity. The results of the calculation and a discussion of the mixing patterns observed, along with some regional calculations, compose section 3. In section 4, we discuss the relationship between the effective diffusivity and the

mean potential vorticity field. We also use  $K_{\text{eff}}$  in conjunction with the potential vorticity field to infer the eddy-driven transport in the ACC region. A discussion of our findings and conclusions are given in section 5.

## 2. Numerical simulation of tracer transport

### a. Southern Ocean state estimate

This study takes advantage of a new, high-resolution Estimating the Circulation and Climate of the Ocean (ECCO) product (<http://www.ecco-group.org>) called the Southern Ocean State Estimate (SOSE; Mazloff 2008). Oceanic state estimation (described, e.g., by Wunsch and Heimbach 2007) rigorously synthesizes diverse observations in a dynamically consistent manner. This is accomplished through minimization of the misfit between the observations and a numerical model, in this case the Massachusetts Institute of Technology general circulation model (MITgcm; Marshall et al. 1997). The observations used to constrain SOSE include Argo subsurface floats, satellite measurements of sea surface temperature and sea surface height, Gravity Recovery and Climate Experiment (GRACE) satellite data, in situ data from CTD and XBT casts, and National Centers for Environmental Prediction (NCEP) reanalysis atmospheric data. The model has a resolution of  $1/6^\circ$ , permitting mesoscale eddies to form, and spans a 2-yr period from 2005 through 2006. During this time period, SOSE is found to be more consistent with the data than optimally interpolated global climatological data products such as the National Oceanic and Atmospheric Administration's (NOAA) *World Ocean Atlas* (Stephens et al. 2001; Gouretski and Koltermann 2004). We use the velocity fields from SOSE to model the evolution of a passive numerical tracer. We also use the mean hydrographic fields to describe the climatological state of the Southern Ocean and to compute potential vorticity. A snapshot of the surface velocity field, revealing SOSE's rich mesoscale structure, is shown in Fig. 1a.

### b. Tracer advection

We characterize the eddy mixing by studying the evolution of a tracer governed by an advection-diffusion equation. The eddies stir the tracer, lengthening its contours and thereby enhancing the effect of small-scale diffusion. Nakamura (1996) developed a method to quantify this process by formulating the tracer equation in terms of a quasi-Lagrangian tracer-area coordinate, in which all transport is diffusive, making it possible to diagnose an effective eddy diffusivity using only a snapshot of the tracer field. Here we use the form given by MSJH, in which the effective diffusivity is written as

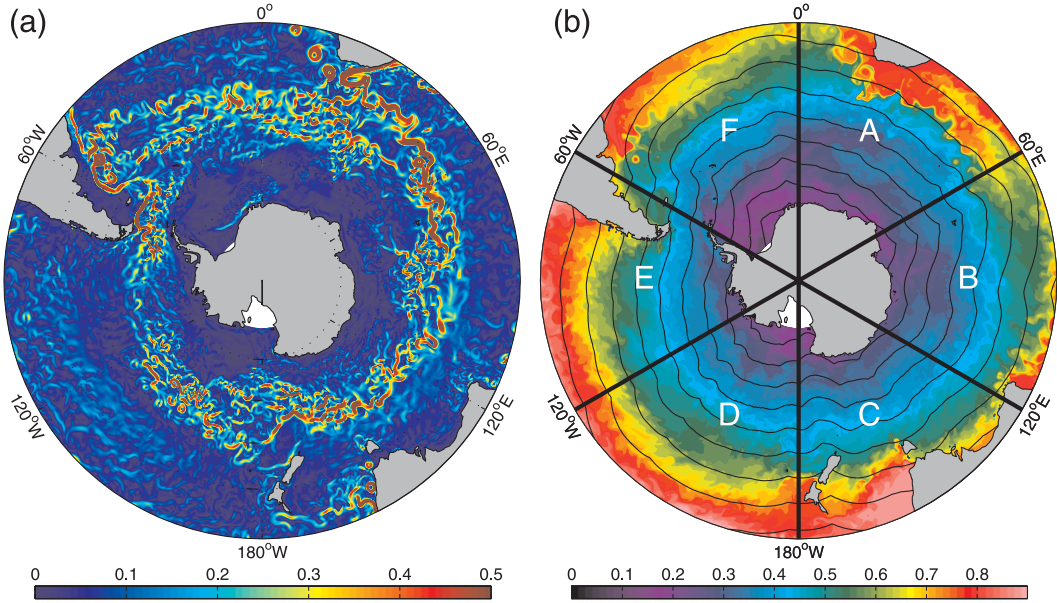


FIG. 1. (a) Snapshot of surface current speed from SOSE. The color scale ranges from 0 to  $0.5 \text{ m s}^{-1}$ . (b) Tracer concentration after 1 yr of advection–diffusion using  $\kappa_h = 50 \text{ m}^2 \text{ s}^{-1}$ . The black contours show the initial tracer distribution, which was also used to define a meridional coordinate for pseudostreamwise averaging. The six sectors highlighted indicate the different regions for the regional effective diffusivity calculations.

$$K_{\text{eff}} = \kappa \frac{L_{\text{eq}}^2}{L_{\min}^2}, \quad (1)$$

where  $\kappa$  represents the small-scale diffusion that halts the cascade of tracer variance,  $L_{\min}$  represents the length of an unstrained contour, and  $L_{\text{eq}}$ , the equivalent length, can be thought of as the length of the stretched contour. This equivalent length can be computed from an instantaneous snapshot of the tracer field as

$$L_{\text{eq}}^2 = \frac{\partial}{\partial A} \int |\nabla^2 q| dA \frac{\left( \frac{\partial q}{\partial A} \right)^2}{\left( \frac{\partial q}{\partial A} \right)^2}. \quad (2)$$

We have included this expression for completeness, but we refer the reader to the appendix of MSJH for its derivation.

The effective diffusivity formalism is rigorously defined for advection–diffusion of a tracer in two dimensions. However, we wish to obtain information about the vertical and meridional distribution of  $K_{\text{eff}}$ . We therefore first employ the SOSE eddying velocity fields  $\mathbf{v} = (u, v, w)$  to advect a passive tracer  $q$  according to the 3D advection–diffusion equation,

$$\frac{\partial q}{\partial t} + \mathbf{v} \cdot \nabla q = \kappa_h \nabla_h^2 q + k_v \frac{\partial^2 q}{\partial z^2}, \quad (3)$$

where  $\kappa_h$  and  $k_v$  are the horizontal and vertical diffusion coefficients and  $\nabla_h^2$  is the horizontal Laplacian. In a second step, the tracer field is then mapped onto two-dimensional neutral surfaces in the interior and  $K_{\text{eff}}$  evaluated from (1) using an appropriate choice of  $\kappa_h$ , as described below.

Following MSJH, we chose an initial tracer distribution approximately aligned with the streamlines of the ACC. As in Karsten and Marshall (2002), a single streamline of the time-mean vertically integrated–transport streamfunction was chosen from the core of the ACC. This was used as a reference to initialize tracer concentrations ranging from 0 to 1 along lines running parallel to this reference contour, as shown in Fig. 1b. The same initial concentration was used on each vertical level. This choice leads to a rapid equilibration of the  $L_{\text{eq}}$  tracer contours, but any initial tracer gradient roughly perpendicular to the ACC would result in a reliable calculation. (This was confirmed by repeating our calculations with the initial tracer contours simply aligned with latitude circles; the resulting  $L_{\text{eq}}$  was not significantly different from the results presented here.) We also employ the contours of this initial tracer field to define an approximate “streamwise average.”

We performed the tracer advection on the same numerical grid as the original SOSE model, using the off-line capability of the MITgcm. With grid points every one-sixth of a degree, the maximum grid spacing was

approximately 18 km. Several experiments were carried out in which  $\kappa_h$  was set to, respectively, 50, 100, 200, and  $400 \text{ m}^2 \text{ s}^{-1}$ . In all cases the vertical diffusion is set to  $\kappa_v = 1 \times 10^{-5} \text{ m}^2 \text{ s}^{-1}$ , roughly consistent with observed diapycnal mixing rates in the thermocline.

The role of diffusive processes inherent in the numerical implementation, together with the overall impact of horizontal versus vertical diffusion, can be assessed by considering the globally averaged tracer variance equation,

$$\frac{1}{2} \frac{\partial \langle q^2 \rangle}{\partial t} = -\kappa_h^{(\text{num})} \langle |\nabla_h q|^2 \rangle - \kappa_v^{(\text{num})} \langle q_z^2 \rangle, \quad (4)$$

where  $\langle \rangle$  indicates a volume-weighted average over the whole domain. Here,  $\kappa_h^{(\text{num})}$  and  $\kappa_v^{(\text{num})}$  represent the diffusivities required to bring the observed decay in  $q^2$  to consistency with the above variance equation. For all values of  $\kappa_h$  in our experiments, the vertical term was at least an order of magnitude smaller than the horizontal, indicating that horizontal diffusion, rather than vertical, is responsible for dissipating tracer variance at small scales. More detailed analysis of the variance equation indicates that, for values of  $\kappa_h$  below  $200 \text{ m}^2 \text{ s}^{-1}$ , implicit numerical diffusion augments the explicit value of  $\kappa_h$  by up to 60%, a finding consistent with incomplete resolution of the Batchelor scale. In particular, using  $\kappa_h = 50 \text{ m}^2 \text{ s}^{-1}$  gave  $\kappa_h^{(\text{num})} = 83 \text{ m}^2 \text{ s}^{-1}$  while  $\kappa_h = 100 \text{ m}^2 \text{ s}^{-1}$  gave  $\kappa_h^{(\text{num})} = 128 \text{ m}^2 \text{ s}^{-1}$ . In these cases, we use the estimated numerical value of  $\kappa_h$  in calculating  $K_{\text{eff}}$ . Higher values of  $\kappa_h$  did not generate significant spurious diffusion.

Before calculating  $K_{\text{eff}}$ , we allowed the tracer to evolve for one year. A sample tracer field after one year of stirring using  $\kappa_h = 50 \text{ m}^2 \text{ s}^{-1}$  is shown in Fig. 1b. Visual inspection reveals plausible tracer patterns and no evidence of gridscale aliasing, despite the rather low value of diffusivity employed. Such levels of explicit diffusivity were also found to be appropriate in the study of MSJH, where altimetric fields were used to drive the tracer evolution rather than, as here, model fields constrained by observations.

### c. Isopycnal projection

The effect of mesoscale eddies acting in the “surface diabatic layer,” where isopycnals outcrop, differs fundamentally from their role in the adiabatic interior of the ocean (Held and Schneider 1999; Kuo et al. 2005). In the surface layer, eddies transport buoyancy horizontally across isopycnals. In the interior, eddies stir primarily along tilted neutral surfaces, mixing potential vorticity and other tracers isopycnally. Here we attempt to characterize these two regions separately, diagnosing

a horizontal  $K_{\text{eff}}$  near the sea surface and an isopycnal  $K_{\text{eff}}^{(i)}$  in the interior.

An individual effective diffusivity calculation requires a two-dimensional tracer field: a slice taken at constant depth for  $K_{\text{eff}}$ , or a slice at constant neutral density for  $K_{\text{eff}}^{(i)}$ . Cross sections can be built by stacking the results from many such slices, as described for example in Nakamura and Ma (1997) and Haynes and Shuckburgh (2000a), who used isentropic surfaces in the atmosphere, or Cerovecki et al. (2009), who employed the same neutral-surface-projection technique described here. Constant-depth tracer fields for computing  $K_{\text{eff}}$  are trivial to extract from the model output, since it uses depth coordinates intrinsically. The neutral-surface projection for  $K_{\text{eff}}^{(i)}$  requires more care. We first calculated neutral density  $\gamma^n$  from the instantaneous SOSE temperature and salinity fields using the algorithm of Jackett and McDougall (1997). We chose 35 discrete values of  $\gamma^n$  to define a new density-based vertical coordinate. The tracer profile at each point was then interpolated onto these values of  $\gamma^n$  and the resulting two-dimensional tracer surfaces analyzed to determine  $K_{\text{eff}}^{(i)}$  as described in the next section.

### 3. Cross sections of effective diffusivity in the meridional plane

Both the theoretical framework for deriving  $K_{\text{eff}}$  in terms of the modified-Lagrangian-mean tracer equation and the numerical technique for its computation are well documented (Nakamura 1996; Nakamura and Ma 1997; Shuckburgh and Haynes 2003; MSJH) and so are not repeated here. We calculated  $L_{\text{eq}}^2$  as defined in (2) using a MATLAB code;  $L_{\text{eq}}^2$  was calculated on both horizontal and isopycnal tracer surfaces from simulations using  $\kappa_h$  values of 50, 100, 200, and  $400 \text{ m}^2 \text{ s}^{-1}$ , yielding a total of eight cross sections. To calculate  $L_{\text{min}}^2$ , the minimum possible length of a tracer contour was inferred by performing an experiment using  $\kappa_h = 4 \times 10^4 \text{ m}^2 \text{ s}^{-1}$ . This very large value of diffusivity decreases the Péclet number to the extent that explicit diffusion rather than advection dominates the tracer evolution. MSJH showed that in this regime, the resulting contour lengths, again calculated from (2), tend to  $L_{\text{min}}$ . Using (1),  $K_{\text{eff}}$  was then computed. As described earlier, the level of mixing experienced by the numerical tracer,  $\kappa_h^{(\text{num})}$ , was diagnosed from the tracer variance equation. A cutoff minimum was imposed on  $L_{\text{min}}$  of 10 000 km, chosen to prevent small values of  $L_{\text{min}}$  (caused by the surface outcropping of isopycnals or by the intersection of topography) from unrealistically inflating  $K_{\text{eff}}$ .

Both  $L_{\text{eq}}$  and  $L_{\text{min}}$  are defined as functions of the area  $A$  enclosed by a tracer contour. A mapping exists between  $A$  and an equivalent latitude  $\phi_e$ . In the atmosphere, in the

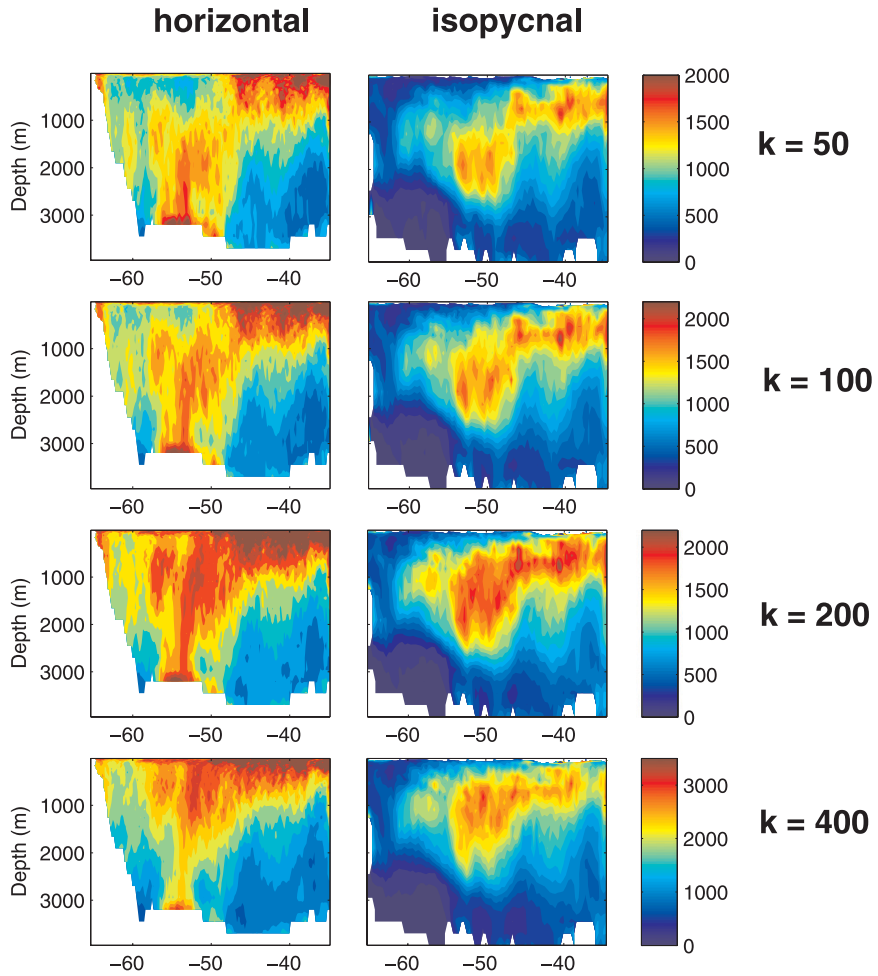


FIG. 2. Comparison of different effective diffusivity calculations. The “horizontal” diffusivities were computed on surfaces of constant height and the isopycnal diffusivities on surfaces of constant neutral density. The same color scale, in  $\text{m}^2 \text{s}^{-1}$ , is used for each value of  $\kappa_h$  indicated on the right. Note that the color scaling changes significantly for  $\kappa_h = 400 \text{ m}^2 \text{s}^{-1}$ .

absence of topography, this mapping simply identifies the latitude circle that encloses the given area. But here we must account for basin geometry as well as isopycnal outcrops. We can define the area enclosed by a latitude circle  $\phi_e$  on a neutral surface  $\gamma^n$  as

$$A_{\gamma^n}(\phi_e) = \int \int_{90^\circ \text{S}}^{\phi_e} g(\lambda, \phi) dA, \quad (5)$$

where  $g(\lambda, \phi) = 0$  for all locations not in the water (i.e., inside topography or beyond isopycnal outcrops) and  $g = 1$  otherwise. We evaluated this expression numerically in the SOSE domain and used it to map  $L_{\text{eq}}$  and  $L_{\text{min}}$  to positions in latitude.

#### a. Global cross section

The results of our calculations for different values of  $\kappa_h$  are shown as meridional cross sections in Fig. 2. (The

isopycnal calculations were mapped back to depth coordinates using the average depth of the neutral surfaces at each latitude.) The horizontal and isopycnal diffusivities share certain characteristics. Each panel in Fig. 2 indicates a region of intense mixing deep beneath the ACC (centered around 54°S) that becomes shallower moving equatorward. The greatest differences between them occur, unsurprisingly, near the surface. The horizontal diffusivities tend to intensify near the surface, at least equatorward of the ACC region, while the isopycnal diffusivities uniformly decrease at depths shallower than 200 m because the sea surface acts to suppress isopycnal stirring on tilted neutral surfaces. The high horizontal effective diffusivities close to the bottom are not the result of enhanced stirring increasing  $L_{\text{eq}}$ , but rather result from the intrusion of topography, which causes small values of  $L_{\text{min}}$  to inflate  $K_{\text{eff}}$ . The isopycnal projections do

not suffer from this problem, and these will be our primary focus.

From Fig. 2, we see that increasing the value of  $\kappa_h$  blurs the structure of  $K_{\text{eff}}$  somewhat. Indeed, visual inspection of the tracer fields reveals that (not surprisingly) they become increasingly smooth and less complex as  $\kappa_h$  is increased. Figure 3 plots horizontal  $K_{\text{eff}}$  at the base of the mixed layer for various choices of  $\kappa_h$ , along with the  $K_{\text{eff}}$  profile obtained by MSJH directly using altimetry. We clearly see that the distributions of  $K_{\text{eff}}$  obtained here using  $\kappa_h = 50$  and  $100 \text{ m}^2 \text{ s}^{-1}$  are very close to those of MSJH, while those obtained using larger values of  $\kappa_h$  are considerably greater in magnitude. Since either of the lower values produces a result consistent with the earlier study, we choose to analyze the  $\kappa_h = 100 \text{ m}^2 \text{ s}^{-1}$  case, because the numerical diffusion ( $\kappa_h^{(\text{num})}$ , diagnosed in the previous section) is smaller in proportion to the explicit diffusion. This choice is also supported on consideration of the  $(\text{Pe}, \text{Nu})$  plot presented in MSJH, where  $\text{Pe}$  is the Péclet number and  $\text{Nu} = K_{\text{eff}}/\kappa_h$  is the Nusselt number. For sufficiently large  $\text{Pe}$  (i.e., sufficiently small  $\kappa_h$ ), the slope of the line in  $(\text{Pe}, \text{Nu})$  space is order unity, in which case  $K_{\text{eff}}$  becomes independent of the small-scale value of  $\kappa_h$  (MSJH; Shuckburgh and Haynes 2003). This decreasing sensitivity can be clearly seen in Fig. 2 as  $\kappa_h$  is reduced.

Since  $K_{\text{eff}}$ , the horizontal diffusivity, applies more readily to eddy buoyancy fluxes in the surface diabatic layer, while  $K_{\text{eff}}^{(i)}$  is more appropriate for isopycnal mixing in the interior, in Fig. 4 we present a composite of these two quantities. We have chosen to separate the regions at 100-m depth, a typical mixed layer depth (MLD) for this region.<sup>1</sup> Contours of the streamwise-averaged zonal velocity are also shown in Fig. 4, indicating the mean position of the ACC. Although the time and spatial average blurs the fine structure and multiple jets of the current, a strong mean flow is still apparent. A striking feature is that in both the surface layer and the interior, effective diffusivity is significantly reduced where the mean flow is strongest. Mixing is enhanced between the 2 and 4  $\text{cm s}^{-1}$  contours, particularly on the equatorward side of the jet: the surface of maximum  $K_{\text{eff}}$  is at a depth of order 1500 m beneath the core of the ACC and shoals on the equatorial flank.

<sup>1</sup> The mixed layer depth provides a reasonable estimate of the actual depth of the surface diabatic layer, since mixed layer waters are subject to convection and thereby exposed to diabatic forcing near the surface. Dong et al. (2008) recently performed a detailed diagnosis of the MLD in the Southern Ocean from Argo data. They found substantial spatial and seasonal MLD variability, with MLDs reaching over 400 m in the winter just north of the Subantarctic Front.

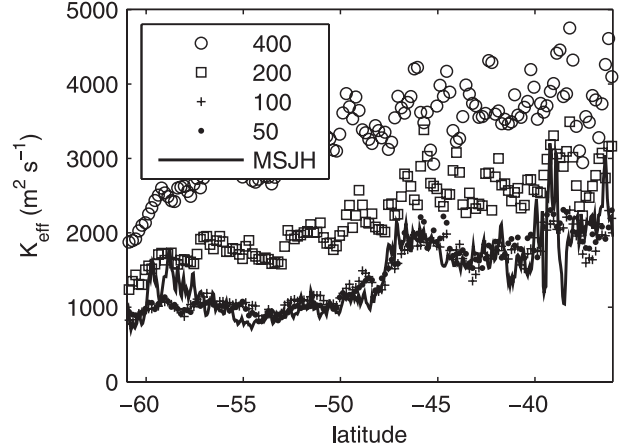


FIG. 3. Comparison of effective diffusivity values with those found by MSJH. The markers show horizontal  $K_{\text{eff}}$  at 100-m depth, roughly at the base of the mixed layer, from our experiments with  $\kappa_h = 400, 200, 100$ , and  $50 \text{ m}^2 \text{ s}^{-1}$ . The solid line is  $K_{\text{eff}}$  from MSJH.

SM anticipated this general form for  $K_{\text{eff}}$ , drawing on insights from linear baroclinic instability theory. In the analysis of a growing baroclinic disturbance (see, e.g., Green 1970; Marshall 1981; Killworth 1997), the diffusivity of quasigeostrophic potential vorticity takes the form

$$K_q = \frac{c_i}{k} \frac{(\frac{1}{2})v'^2}{(U - c_r)^2}, \quad (6)$$

where  $U$  is the mean zonal current,  $c_r$  is the real part of the phase speed,  $c_i$  is the imaginary part (the growth rate),  $k$  is the zonal wavenumber, and  $(\frac{1}{2})v'^2$  is the eddy kinetic energy. At finite amplitude, the general dependence of the diffusivity on the eddy kinetic energy, the phase speed, and the mean flow can be expected to hold, since the form of the diffusivity is related to the kinematics of particle displacement. SM noted that the observed zonal propagation speed of altimetric signals in the ACC was roughly  $2 \text{ cm s}^{-1}$ , significantly smaller than mean surface zonal currents, typically  $10 \text{ cm s}^{-1}$  (e.g., shown in Fig. 4). At depth, however, where mean flow advection and wave propagation speeds are much more closely in sync, the wave can “keep up” with the mean flow and achieve large meridional excursions of fluid parcels, promoting mixing. SM followed up these linear arguments with detailed, fully turbulent calculations using a stacked quasi-geostrophic model, which was relaxed back to observed hydrography on the large scale. They confirmed that intensified mixing of potential vorticity occurred at depth, near the steering level predicted by linear theory where  $U = c$ . The depth where  $U = c$  is also frequently referred to as a “critical level” or “critical layer” (Bretherton 1966; Boss and

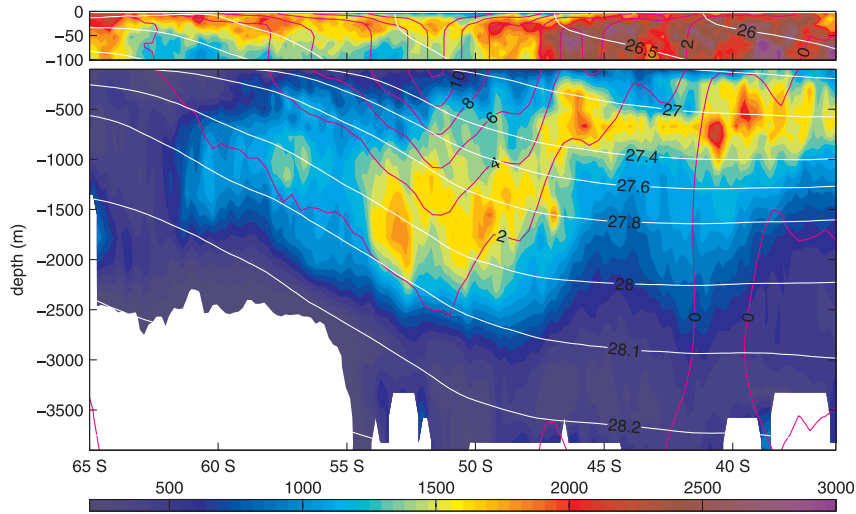


FIG. 4. Effective diffusivity  $K_{\text{eff}}$  in  $\text{m}^2 \text{s}^{-1}$ . (top) Horizontal effective diffusivity in the upper 100 m. In this region the diffusivity can be interpreted as a horizontal eddy mixing in the mixed layer. (bottom) Isopycnal effective diffusivity, which characterizes the mixing of passive tracers such as PV in the ocean interior. The magenta contour lines show the streamwise-averaged zonal velocity, indicating the position of the mean jet of the ACC, and mean isopycnals appear in white. The velocity contour interval is  $2 \text{ cm s}^{-1}$ .

Thompson 1999). The findings reported here, which make use of a much more realistic eddying model constrained to be close to observations, support the idea that critical-layer enhancement occurs in the region of the ACC. The numerical studies of Treguier (1999) and Cerovecki et al. (2009) also provide clear evidence of intensified mixing in the critical layer of a baroclinically unstable jet. Treguier (1999) in particular diagnoses mixing coefficients based on flux-gradient inversions of both quasigeostrophic potential vorticity in the horizontal and Ertel potential vorticity along isopycnals. The resulting vertical diffusivity profile (her Fig. 9) is remarkably similar to our vertical profile of  $K_{\text{eff}}^{(i)}$  in the jet axis, reaching a peak of  $1600 \text{ m}^2 \text{s}^{-1}$  at 1500-m depth.

If steering-level effects are responsible for the enhanced diffusivity at depth, we might expect to observe eddies propagating eastward at a speed slower than the surface mean flow in SOSE. The phase speeds can be calculated using Radon transforms, as done in SM, but here we opt for the simpler approach of constructing Hovmöller diagrams. We examined the SOSE sea surface height anomaly in a sector in the Pacific between  $165^\circ$  and  $135^\circ\text{W}$ . Figure 5 shows two Hovmöller diagrams, one at  $53^\circ\text{S}$ , near the mean zonal flow maximum in this region, and one at  $47^\circ\text{S}$ . It is encouraging to see that  $c \simeq 2 \text{ cm s}^{-1}$  in the ACC, since this places the steering level around 2000 m deep, in agreement with the structure of  $K_{\text{eff}}$  in Fig. 4. North of the jet at  $47^\circ\text{S}$ , the anomalies propagate westward at approximately  $1 \text{ cm s}^{-1}$ . These numbers are in agreement with those of SM.

### b. Regional cross sections

While the global cross section of effective diffusivity seems to offer a picture consistent with the global streamwise-average mean fields, the Southern Ocean contains large zonal asymmetries in bathymetry, circulation, and eddy activity. To address the zonal variations in mixing, we split the domain into six sectors and repeated the calculation on each sector. Shuckburgh et al. (2009b) have shown how this procedure, while not formally permitted in Nakamura's construction, still gives meaningful values of  $K_{\text{eff}}$  in the truncated domain. The cross sections of the isopycnal diffusivity  $K_{\text{eff}}^{(i)}$  are shown in Fig. 6, along with zonally averaged zonal velocity and isopycnals. Again, we imposed a minimum on  $L_{\min}$ , requiring  $L_{\min} > 2200 \text{ km}$  in each sector. Where  $L_{\min}$  does not meet this criterion, no value is plotted in Fig. 6, leading to the irregular white patches near the surface and bottom. Outcropping isopycnals or the intersection of neutral surfaces with bottom topography can lead to very small values of  $L_{\min}$ , but this effect does not truly reflect an enhanced effective diffusivity. The cutoff procedure focuses attention on variations in  $K_{\text{eff}}$  due to variation in  $L_{\text{eq}}$ .

Intensified mixing at depth is clearly present on the flanks of the jet maxima in most sectors, the location in latitude varying with the local flow. Other regions of enhanced mixing in each sector can also be related to the local current system. In particular, as noted by Shuckburgh et al. (2009b), strong mixing is found in regions where

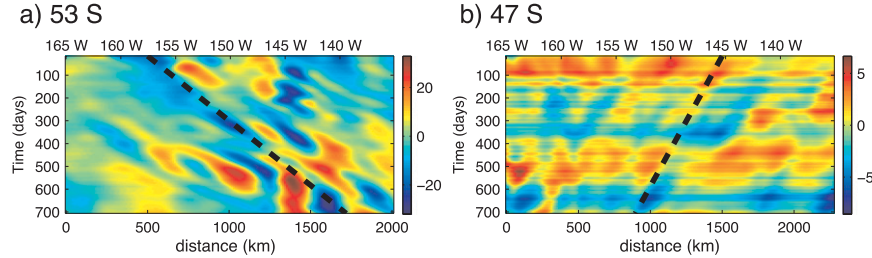


FIG. 5. Hovmöller diagrams of SOSE sea surface height anomaly (cm) in the Pacific. (a) At 53°S, a latitude where the ACC is strong in this sector, the anomalies appear to propagate east, downstream. The dotted black line denotes an eastward phase speed of  $2 \text{ cm s}^{-1}$ . (b) At 47°S, north of the ACC, the anomalies propagate west, as expected of Rossby waves in the absence of a strong mean zonal flow. The dotted line here indicates a westward phase speed of  $1 \text{ cm s}^{-1}$ . Note that the anomalies in the northern region are much weaker than those in the ACC, and consequently, variability on short time scales is visible in (b) that is not noticeable in (a) due to the difference in color scales.

eddies are generated in association with topographic features in regions of weak zonal mean flow. In Fig. 6a, of the region south of Africa between the Atlantic and Pacific, the mixing in the ACC is concentrated in a narrow region below and equatorward of the jet. Another surface-intensified mixing region appears north of 40°S. Movies of the tracer evolution suggest that this mixing is associated with the intense eddies of the Agulhas rings. The Indian Ocean sector, Fig. 6b, shows very strong mixing on both sides of the jet as well as below. This sector contains the Kerguelen Plateau, a large topographic feature that generates strong eddy activity as the flow passes over and around it. South of Australia (Fig. 6c), the only strong mixing occurs in a deep, narrow band between 1000- and 2000-m depth. Figure 6d is the southwest Pacific, the region in which the Hovmöller diagrams of Fig. 5 were constructed. In agreement with our steering-level hypothesis, enhanced mixing at depth is observed at around 53°S below the jet where the zonal velocity is  $2 \text{ cm s}^{-1}$ . This sector also shows the clearest multiple-jet structure, both in the mean flow field and in the bands of high and low  $K_{\text{eff}}$ . In Fig. 6e, the southeast Pacific,  $K_{\text{eff}}$  seems quite weak, consistent with the low eddy kinetic energy in this region and with the results of Shuckburgh et al. (2009b). However, it still shows intensification with depth. Finally, downstream of Drake Passage (Fig. 6f), intense mixing appears very widespread. It is likely that much of the mixing north of 45°S is the result of eddies spawned by the Falkland Current. In general, the regional plots suggest that much of the strong mixing visible in Fig. 4 north of 45°S, where the mean flow is very weak, is the result of interaction with the continents rather than frontal dynamics.

The Diapycnal and Isopycnal Mixing Experiment in the Southern Ocean (DIMES; Gille et al. 2007) is ongoing (2009–12). The goal of the experiment is to mea-

sure mixing rates in the region upstream of the Drake Passage using RAFOS floats and a patch of chemical tracer. Our results predict that isopycnal mixing rates vary considerably with latitude and depth. To gain some insight into the locations of intensified mixing in the DIMES region, we can map the effective diffusivity *back* onto tracer contours from the tracer snapshot used in the  $K_{\text{eff}}$  calculation, since  $K_{\text{eff}} = K_{\text{eff}}(A) = K_{\text{eff}}(q)$ . We have constructed such maps on the two DIMES target isopycnals,  $\gamma'' = 27.2$  and  $\gamma'' = 27.9$ , and near the surface, in Fig. 7. (These isopycnals are also highlighted in Fig. 6e, the sector containing the DIMES region.) Satellite altimetric data are available to the DIMES investigators in real time during the deployment of floats and tracers. With this in mind, we have included contours of the instantaneous sea surface height from SOSE in Fig. 7, which suggest the position of the ACC fronts. This presentation highlights the fact that isopycnal mixing on the deeper surface is strongest directly at the front, while on the shallower surface the mixing is weak right at the front, but stronger to the north.

#### 4. Potential vorticity mixing

The meridional overturning circulation cannot be measured directly and must be inferred. One approach in the Southern Ocean, where eddies are suspected to contribute significantly to the meridional transport, has been to deduce the eddy mass transport by assuming the down-gradient transfer of potential vorticity by eddies. For instance, Marshall et al. (1993), Speer et al. (2000), and Karsten and Marshall (2002) have all employed some version of this technique. To use this approach, a diffusion coefficient of PV must be specified; in many cases, this coefficient is assumed to be constant. We have found, however, that isopycnal mixing is highly nonuniform in

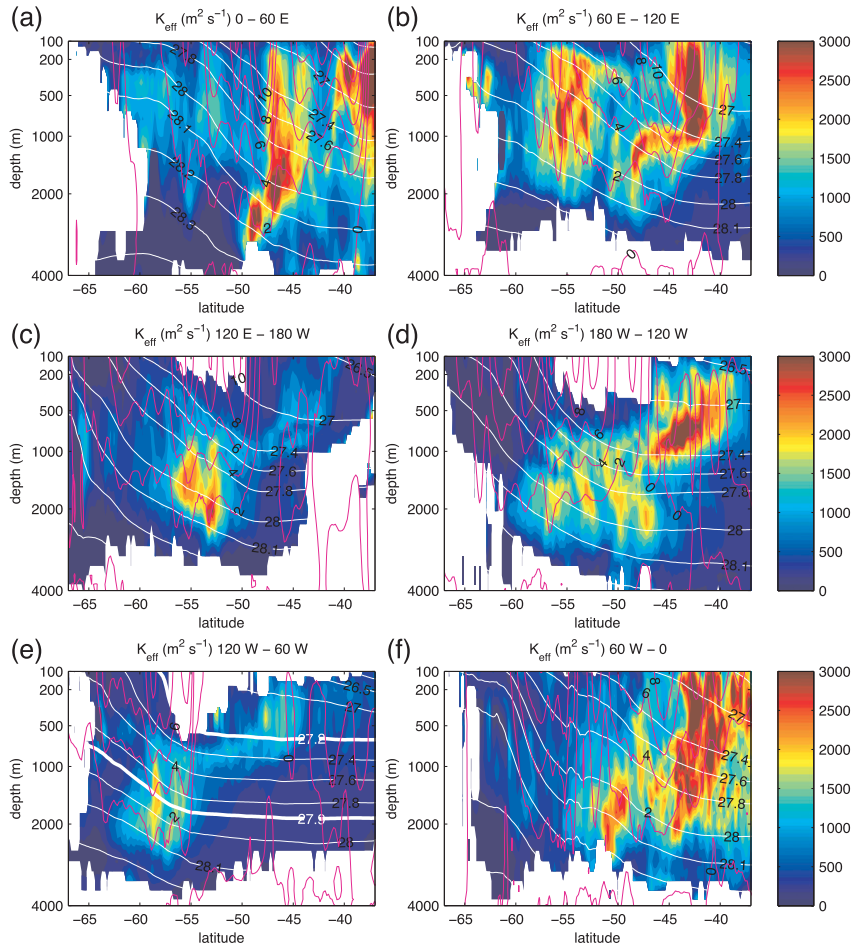


FIG. 6. Regional cross sections of isopycnal  $K_{\text{eff}}$ . The magenta contour lines show the zonally averaged zonal flow, with a contour interval of  $2 \text{ cm s}^{-1}$ . The mean isopycnals appear in white. The sectors are (a)  $0^\circ$ – $60^\circ\text{E}$ , (b)  $60^\circ$ – $120^\circ\text{E}$ , (c)  $120^\circ\text{E}$ – $180^\circ$ , (d)  $180^\circ$ – $120^\circ\text{W}$ , (e)  $120^\circ$ – $60^\circ\text{W}$ , and (f)  $60^\circ\text{W}$ – $0^\circ$ . The DIMES experiment will take place mostly in (e).

space. In this section we explore some of the consequences of spatial variations in effective diffusivity. Note that we do not attempt to directly diagnose the eddy PV flux or flux-gradient relationships from SOSE because the computation of stable eddy statistics demands long time series (only two years are available from SOSE) and because the local fluxes are dominated by rotational components (Marshall and Shutts 1981).

#### a. The potential vorticity field

We diagnosed the potential vorticity distribution using the time-mean SOSE fields. The following form is computed appropriate to the large scale:

$$P = f \frac{\partial b}{\partial z}, \quad (7)$$

where  $b$  is the buoyancy and  $f$  the Coriolis parameter. The relative vorticity has been neglected because the

Rossby number is small on the large scales. Using the same isopycnal transformation described in section 2, we computed  $P$  and took its streamwise average in buoyancy space (i.e., following streamlines *and* isopycnals). The result is plotted, transformed back to depth coordinates, in Fig. 8a. We see that surfaces of constant  $b$  and surfaces of constant  $P$  align with one another over much of the domain, especially for isopycnals that do not outcrop. This is confirmed by the plot of the isopycnal gradient of  $P$  shown in Fig. 8b, which is small in much of the interior. Notably, PV gradients become very large near the surface in the southern ACC region, just where we observe reduced effective diffusivities. To examine this more closely, in Fig. 9 we plot the PV gradient along with  $K_{\text{eff}}^{(i)}$  on several different isopycnals. We do indeed find consistently low values of  $K_{\text{eff}}^{(i)}$  where PV gradients are low. The PV gradients are high in the core of the jet, consistent with the invertibility

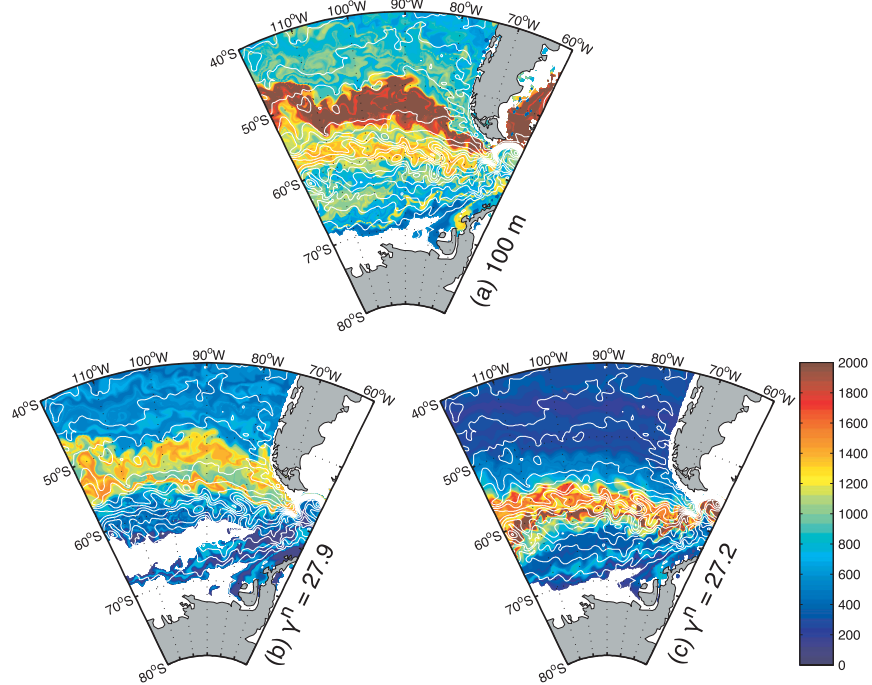


FIG. 7. Maps of effective diffusivity in the region of the DIMES experiment. (a) Horizontal effective diffusivity at 100-m depth; isopycnal effective diffusivity on neutral surfaces (b)  $\gamma^n = 27.2$  and (c)  $\gamma^n = 27.9$ . A snapshot of sea surface height from SOSE from the same time is overlaid, with contour levels of 10 cm.

principle, and in this region the effective diffusivity is smaller. Where the PV gradient is very weak, no amount of mixing can lead to a PV flux. But there does appear to be a transition zone, where both  $(\partial P/\partial y)_b$  and  $K_{\text{eff}}$  are nonzero. This suggests a nonzero eddy flux of PV.

### b. Parameterized eddy forcing

We consider the streamwise- and time-average momentum balance of the large-scale flow through the transformed Eulerian mean (TEM) zonal momentum equation (see, e.g., Andrews et al. 1987; Ferreira et al. 2005):

$$-fv_{\text{res}} = -\frac{1}{\rho_0} \frac{\partial \bar{P}}{\partial x} + \bar{v}'q' + \frac{1}{\rho_0} \frac{\partial \bar{\tau}_x^w}{\partial z}, \quad (8)$$

where  $v_{\text{res}}$  is the residual meridional velocity, a sum of eddy and mean contributions,  $\bar{v}'q'$  is the zonal- or streamwise-average meridional eddy QGPV flux, and  $\bar{\tau}_x^w$  is the wind stress. It is common to define an “eddy velocity”  $v^*$  as the ageostrophic part explicitly balanced by the PV flux:

$$-fv^* = \bar{v}'q'. \quad (9)$$

The quantity  $v^*$  is often referred to as the bolus velocity, and is also related to the “gyroscopic pump” described by Dritschel and McIntyre (2008).

Following, for example, Green (1970), Rhines and Young (1982), Killworth (1997), Visbeck et al. (1997), and Treguier et al. (1997), etc., we assume  $\bar{v}'q'$  is transferred down the mean gradient  $\bar{q}_y$  with our isopycnal effective diffusivity, thus

$$\bar{v}'q' = -K_{\text{eff}}^{(i)} \frac{\partial \bar{q}}{\partial y}. \quad (10)$$

Note that the isopycnal effective diffusivity is used in Eq. (10) and is worthy of comment. As shown by Plumb and Ferarri (2005), in the limit that relative vorticity can be neglected, the *residual* meridional isentropic eddy flux of Ertel PV is proportional to the horizontal meridional eddy flux of QGPV. Indeed we note in passing that, under quasigeostrophic scaling, the meridional gradient of QGPV at constant  $z$  is equal to the meridional gradient of Ertel potential vorticity  $P$  along isopycnals, that is,

$$\left( \frac{\partial q}{\partial y} \right)_z \simeq \frac{1}{N^2} \left( \frac{\partial P}{\partial y} \right)_b. \quad (11)$$

We checked this relation in SOSE and found it to hold well everywhere outside of the mixed layer. Thus (8) and (10), written in height coordinates, are not as restrictive as

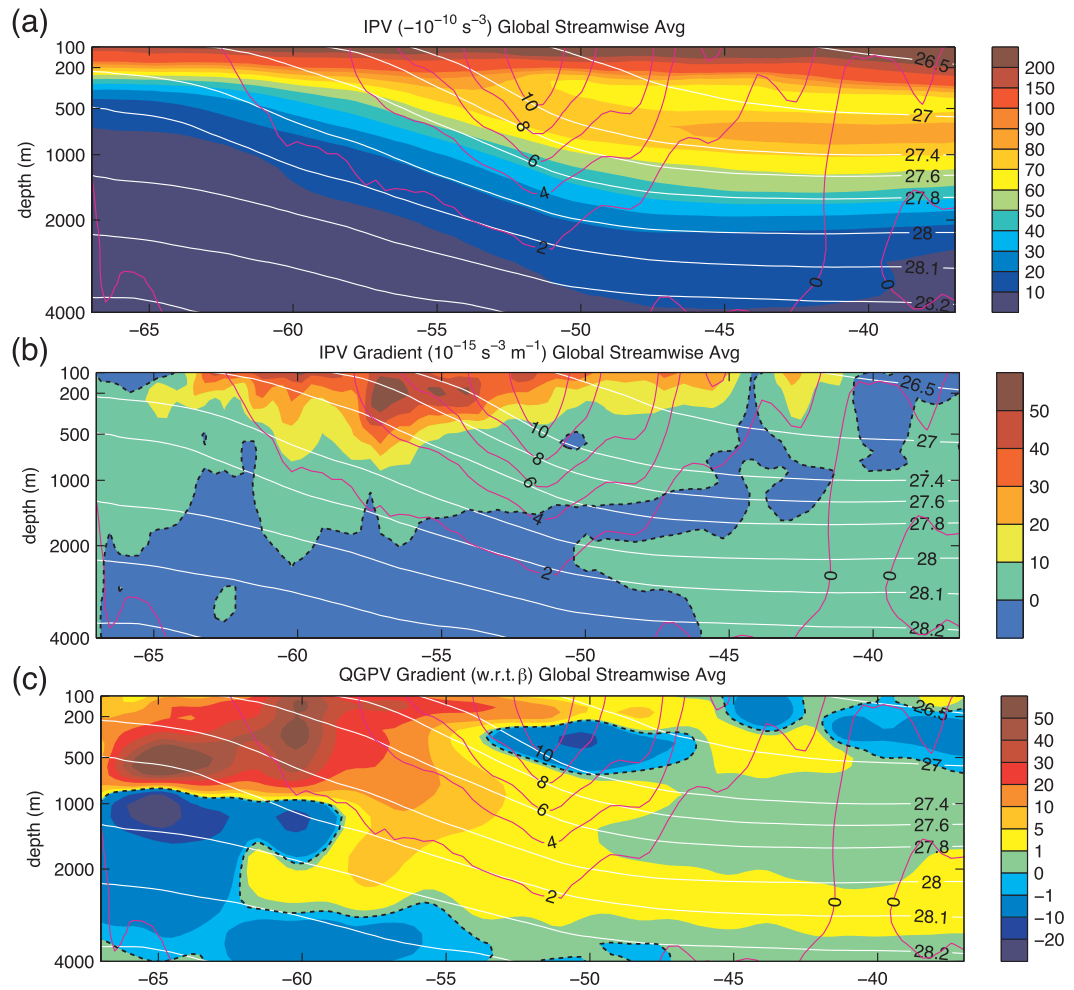


FIG. 8. (a) Streamwise-averaged IPV as defined by (7). The units are  $-10^{10} \text{ s}^{-3}$ . (The PV is negative everywhere, but we have reversed the sign for clarity.) The magenta contours (interval  $2 \text{ cm s}^{-1}$ ) show the streamwise-averaged zonal flow, denoting the mean position of the ACC. (b) Streamwise-averaged IPV gradient; units:  $10^{-15} \text{ s}^{-3} \text{ m}^{-1}$ . (c) Streamwise-averaged QGPV gradient, as defined by (12), normalized with respect to the mean value of  $\beta$  in the domain.

they may seem: they are isomorphic, both mathematically and physically, to analogous expressions in isopycnal coordinates. Since our isopycnal effective diffusivities most closely describe the transport of a conserved tracer (like Ertel PV) along isopycnals,  $K_{\text{eff}}^{(t)}$  is the more appropriate choice to capture the horizontal eddy mixing of QGPV.

The mean QGPV gradient was computed at each latitude. Neglecting the relative vorticity gradient, which is very small compared to the other terms, the gradient takes the form

$$\frac{\partial \bar{q}}{\partial y} = \frac{\partial}{\partial y} \left[ f_0 + \beta y + \frac{\partial}{\partial z} \left( \frac{f_0}{N^2} \bar{b} \right) \right] = \beta - f_0 \frac{\partial s}{\partial z}, \quad (12)$$

where  $s = -\bar{b}_y/N^2$  is the mean isopycnal slope. We allow  $\beta$  and  $f_0$  to take on local values at each latitude,

assuming the scaling assumptions of QG theory to be locally valid, as in, for example, Smith (2007). Numerical implementation requires much differentiation and can lead to noise on the grid scale that was removed using a Shapiro filter. The streamwise-averaged  $\bar{q}_y$  is shown in Fig. 8c. Its general structure—the large positive gradient south of the ACC near the surface, and the locations of negative gradients—is similar to the isentropic potential vorticity gradient (IPVG), as expected.

We can use the parameterization of (10), along with (9), to estimate the eddy velocity  $v^*$ . We can then compare this estimate with one based on a constant diffusivity  $K = 1000 \text{ m}^2 \text{ s}^{-1}$ , similar to the conventional Gent–McWilliams parameterization. The results of such an estimate are shown in Fig. 10 at two different latitudes in the ACC. In general, the profiles show southward eddy

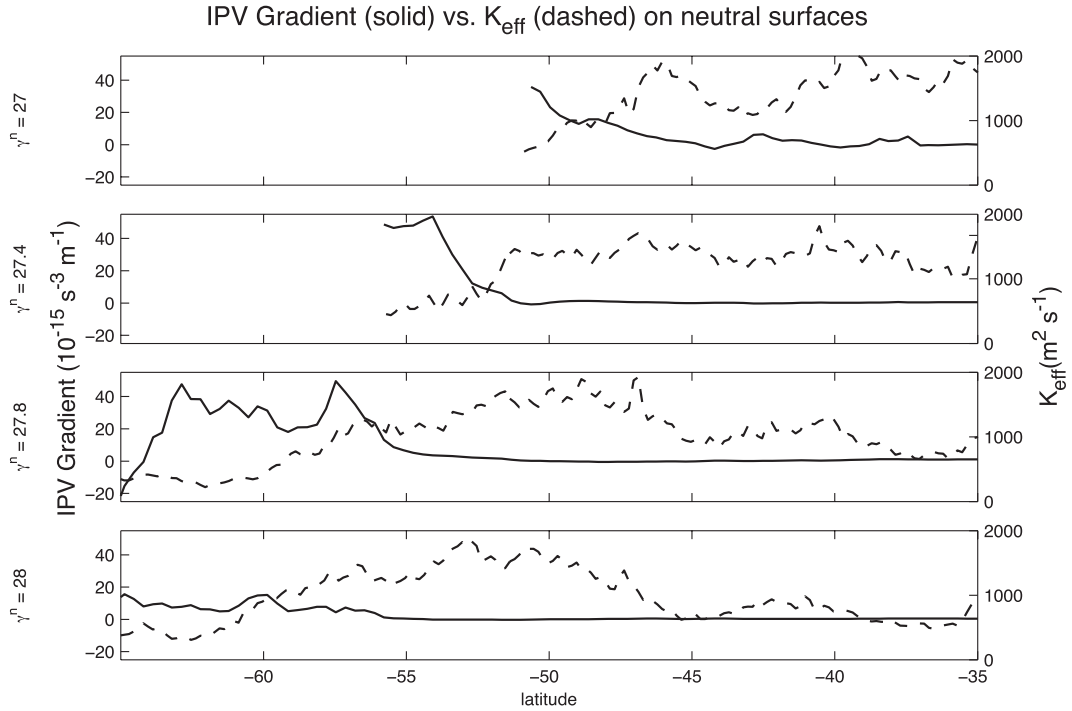


FIG. 9. The effective isopycnal diffusivity [ $K_{\text{eff}}^{(i)}$ ; solid lines] and the IPVG (dashed lines) on several different neutral surfaces:  $\gamma^n$  = (top to bottom) 27.0, 27.4, 27.8, and 28.0. Only values where the mean isopycnal depth is greater than 100 m have been plotted. Weaker interior IPVGs correspond with higher effective diffusivities and vice versa.

transport above 1000 m and, in some cases, weaker northward transport at depths. This circulation is consistent with the effort by the eddies to flatten the sloping isopycnals, releasing potential energy. Below 1000-m depth, where the PV gradients are weaker and  $K_{\text{eff}}$  is relatively high, the two methods of estimating  $v^*$  yield very similar estimates. But at shallower depths, the constant- $K$  parameterization produces a much greater estimate of the southward eddy transport in the density classes corresponding to upper-circumpolar deep water ( $27.5 < \gamma^n < 28.0$ ). From this we conclude that one potential consequence of the diminished mixing in the jet core is the suppression of the eddy component of the meridional overturning circulation.

## 5. Discussion and conclusions

This study has used a tracer-based approach, together with a model of the Southern Ocean constrained by observations, to quantify mesoscale eddy stirring in the Southern Ocean. The foremost result we wish to highlight is the presence of enhanced eddy effective diffusivity well below 1000-m depth in the Southern Ocean. Overall, a structure is observed of reduced eddy diffusivity at the core of the ACC, with enhanced values on its flanks and at depth where the zonal ve-

locity is in the range of 2–4  $\text{cm s}^{-1}$ . We suggest that this is strongly indicative of mixing at a critical layer. These findings are consistent with the quasigeostrophic analysis of SM and the idealized models of Cerovecki et al. (2009) and Treguier (1999), with theoretical considerations based on the observed reversal of potential vorticity gradients and the steering level of linear baroclinic modes, and with basic kinematics. While we have focused on the mixing of PV, it is important to keep in mind that the effective diffusivities diagnosed here apply to the mixing of any tracer, be it chemical or biological.

Shuckburgh et al. (2009a) and Sallée et al. (2008) noted that at the surface, assessments of eddy mixing based on particle dispersion do not indicate a minimum at the core of the ACC. Finite-time Lyapunov exponents, another possible measurement of eddy stirring, correlate closely with eddy kinetic energy but do not seem to be diminished by strong mean flow, reaching their highest values in the western boundary currents and ACC (Waugh and Abraham 2008; Shuckburgh et al. 2009a,b). Similarly, particle-based results do not seem to indicate enhanced mixing below the ACC at depth (A. Griesel et al. 2009, unpublished manuscript). In light of the upcoming DIMES experiments, it is important to reconcile these views of eddy mixing. Some progress has been made on this front by d’Ovidio et al. (2009).

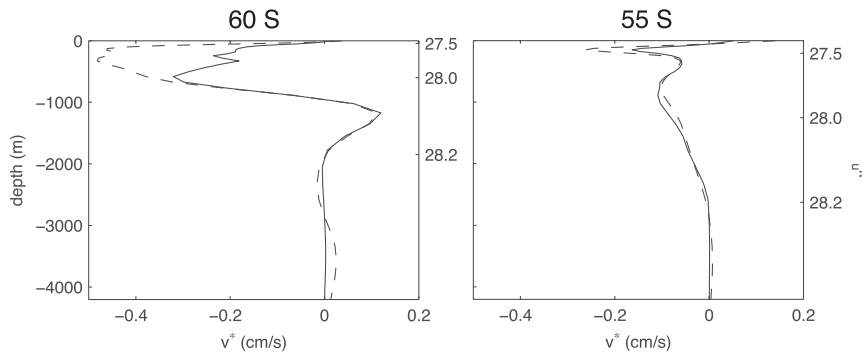


FIG. 10. Estimated eddy-induced velocities  $v^*$  based on (9) and (10) at two different latitudes (left)  $60^\circ$  and (right)  $55^\circ\text{S}$  in the ACC derived from the SOSE mean fields. The solid lines indicate  $K_{\text{eff}}^{(i)}$  was used as the QGPV diffusivity, while the dashed lines are for a constant diffusivity  $K = 1000 \text{ m}^2 \text{ s}^{-1}$ . Isopycnal depths for each profile are indicated on the rhs of each panel.

We argue that effective diffusivity is a useful metric because of the dynamically consistent relationship it holds with the IPV gradient. The strong IPV gradient in the core of the ACC acts as a barrier to wave propagation—baroclinically unstable waves propagating in the steering level on the edge of this gradient break, form closed eddies, and homogenize the low-PV region equatorward of the jet. This conceptual picture bears a close resemblance to the winter stratosphere, where high effective diffusivities in the “surf zone” outside the polar vortex are indicative of breaking planetary waves (Haynes and Shuckburgh 2000a). However, several important distinctions complicate this interpretation. The size of mesoscale eddies in the Southern Ocean is far below the planetary scale. Indeed, the streamwise-averaged view necessarily obscures localized eddy processes such as interactions with particular topographical features (e.g., the Kerguelen Plateau). This point is underscored by the wide variations seen in the effective diffusivity patterns between sectors. Second, planetary waves in the stratosphere are generally thought to propagate up from the troposphere (McIntyre and Palmer 1983), far below the critical layer they encounter in the stratosphere. There is no such spatial separation in the ACC. The eddies arise as a result of baroclinic instability and interact with the critical layer in the same region. Perhaps a better atmospheric analogy is the midlatitude troposphere, where intense mixing at the steering level homogenizes PV and brings the mean state closer to neutrality. This process has been studied in the context of baroclinic adjustment (Stone 1978; Zurita-Gotor and Lindzen 2004a,b). Another open question is the relationship between this large-scale mixing structure and the smaller-scale multiple jets of the ACC. Thompson (2010) recently conducted an analysis of mixing and multiple-jet formation over topography with an eye to the ACC; he found re-

gions of enhanced mixing between each of the small-scale jets. How these small-scale mixing patterns influence the large scale is an important question for future investigation.

We have used effective diffusivity profiles to estimate eddy-induced meridional velocities by parameterizing the eddy QGPV flux. This produced a reasonable picture; the sense and magnitude of the circulation were consistent with other inferences and models. The parameterization using effective diffusivity was compared to a constant diffusivity assumption, as in the Gent–McWilliams parameterization. We found the greatest differences to arise from the low values of  $K_{\text{eff}}$  in the ACC core and on its poleward flank, rather than from the high values of  $K_{\text{eff}}$  found near the steering level, where weak PV gradients dominate. While not quantitatively rigorous, these estimates show how the transport barrier in the core of the jet could potentially affect the strength of the meridional overturning circulation. We conclude that the consequences of the variations of the effective diffusivity for the large-scale overturning circulation merit further study.

**Acknowledgments.** Helen Hill provided crucial help with the numerical models. We also thank Raffaele Ferrari and Alan Plumb for their helpful feedback and guidance. Two anonymous reviewers greatly improved the manuscript with their suggestions. This study was supported by the Polar Programs division of the National Science Foundation.

## REFERENCES

- Andrews, D., J. Holton, and C. Leovy, 1987: *Middle Atmosphere Dynamics*. International Geophysical Series, Vol. 40, Academic Press, 489 pp.

- Boss, E., and L. Thompson, 1999: Lagrangian and tracer evolution in the vicinity of an unstable jet. *J. Phys. Oceanogr.*, **29**, 288–304.
- Bower, A. S., 1991: A simple kinematic mechanism for mixing fluid parcels across a meandering jet. *J. Phys. Oceanogr.*, **21**, 173–182.
- , and T. Rossby, 1989: Evidence of cross-frontal exchange processes in the Gulf Stream based on isopycnal RAFOS float data. *J. Phys. Oceanogr.*, **19**, 1177–1190.
- , H. T. Rossby, and J. L. Lillibridge, 1985: The Gulf Stream—Barrier or blender? *J. Phys. Oceanogr.*, **15**, 24–33.
- Bretherton, F. P., 1966: Critical layer instability in baroclinic flows. *Quart. J. Roy. Meteor. Soc.*, **92**, 325–334.
- Cerovecki, I., R. A. Plumb, and W. Heres, 2009: Eddy transport and mixing in a wind- and buoyancy-driven jet on the sphere. *J. Phys. Oceanogr.*, **39**, 1133–1149.
- Dong, S., J. Sprintall, S. Gille, and L. Talley, 2008: Southern Ocean mixed-layer depth from Argo float profiles. *J. Geophys. Res.*, **113**, C06013, doi:10.1029/2006JC004051.
- d'Ovidio, F., E. Shuckburgh, and B. Legras, 2009: Local mixing events in the upper troposphere and lower stratosphere. Part I: Detection with the Lyapunov diffusivity. *J. Atmos. Sci.*, **66**, 3678–3694.
- Dritschel, D. G., and M. McIntyre, 2008: Multiple jets as PV staircases: The Phillips Effect and the resilience of eddy transport barriers. *J. Atmos. Sci.*, **65**, 855–875.
- Esler, J. G., 2008a: Robust and leaky transport barriers in unstable baroclinic flows. *Phys. Fluids*, **20**, 116602, doi:10.1063/1.3013631.
- , 2008b: The turbulent equilibration of an unstable baroclinic jet. *J. Fluid Mech.*, **599**, 241–268.
- Ferreira, D., J. Marshall, and P. Heimbach, 2005: Estimating eddy stresses by fitting dynamics to observations using a residual-mean ocean circulation model and its adjoint. *J. Phys. Oceanogr.*, **35**, 1891–1910.
- Gille, S. T., K. Speer, J. R. Ledwell, and A. C. Naveira-Garabato, 2007: Mixing and stirring in the Southern Ocean. *Eos, Trans. Amer. Geophys. Union*, **88**, doi:10.1029/2007EO390002.
- Gouestski, V., and K. Koltermann, 2004: WOCE global hydrographic climatology. Tech. Rep., Berichte des Bundesamtes für Seeschiffahrt und Hydrographie, 52 pp.
- Green, J. S., 1970: Transfer properties of the large-scale eddies and the general circulation of the atmosphere. *Quart. J. Roy. Meteor. Soc.*, **96**, 157–185.
- Greenslade, M. D., and P. Haynes, 2008: Vertical transition in transport and mixing in baroclinic flows. *J. Atmos. Sci.*, **65**, 1137–1158.
- Haynes, P., and E. Shuckburgh, 2000a: Effective diffusivity as a diagnostic of atmospheric transport. Part I: Stratosphere. *J. Geophys. Res.*, **105**, 22 777–22 794.
- , and —, 2000b: Effective diffusivity as a diagnostic of atmospheric transport. Part II: Troposphere and lower stratosphere. *J. Geophys. Res.*, **105**, 795–810.
- , D. A. Poet, and E. Shuckburgh, 2007: Transport and mixing in kinematic and dynamically consistent flows. *J. Atmos. Sci.*, **64**, 3640–3652.
- Held, I., and T. Schneider, 1999: The surface branch of the zonally averaged mass transport circulation in the troposphere. *J. Atmos. Sci.*, **56**, 1668–1697.
- Jackett, D., and T. McDougall, 1997: A neutral density variable for the world's oceans. *J. Phys. Oceanogr.*, **27**, 237–263.
- Karsten, R. H., and J. Marshall, 2002: Constructing the residual circulation of the ACC from observations. *J. Phys. Oceanogr.*, **32**, 3315–3327.
- Killworth, P. D., 1997: On the parameterization of eddy transfer: Part I: Theory. *J. Mar. Res.*, **55**, 1171–1197.
- Kuo, A., R. A. Plumb, and J. Marshall, 2005: Transformed Eulerian-mean theory. Part II: Potential vorticity homogenization and equilibrium of a wind- and buoyancy-driven zonal flow. *J. Phys. Oceanogr.*, **35**, 175–187.
- Marshall, J., 1981: On the parameterization of geostrophic eddies in the ocean. *J. Phys. Oceanogr.*, **11**, 1257–1271.
- , and G. Shutts, 1981: A note on rotational and divergent eddy fluxes. *J. Phys. Oceanogr.*, **11**, 1677–1681.
- , D. Olbers, H. Ross, and D. Wolf-Gladrow, 1993: Potential vorticity constraints on the dynamics and hydrography of the Southern Ocean. *J. Phys. Oceanogr.*, **23**, 465–487.
- , A. Adcroft, C. Hill, L. Perelman, and C. Heisey, 1997: A finite-volume, incompressible Navier–Stokes model for studies of the ocean on parallel computers. *J. Geophys. Res.*, **102**, 5753–5766.
- , E. Shuckburgh, H. Jones, and C. Hill, 2006: Estimates and implications of surface eddy diffusivity in the Southern Ocean derived from tracer transport. *J. Phys. Oceanogr.*, **36**, 1806–1821.
- Mazloff, M., 2008: The Southern Ocean meridional overturning circulation as diagnosed from an eddy permitting state estimate. Ph.D. thesis, Massachusetts Institute of Technology, 127 pp.
- McIntyre, M., and T. Palmer, 1983: Breaking planetary waves in the stratosphere. *Nature*, **305**, 593–600.
- Nakamura, N., 1996: Two-dimensional mixing, edge formation, and permeability diagnosed in an area coordinate. *J. Atmos. Sci.*, **53**, 1524–1537.
- , and J. Ma, 1997: Modified Lagrangian-mean diagnostics of the stratospheric polar vortices 2. Nitrous oxide and seasonal barrier migration in the cryogenic limb array etalon spectrometer and SKYHI general circulation model. *J. Geophys. Res.*, **102**, 25 721–25 735.
- Plumb, R. A., and R. Ferrari, 2005: Transformed Eulerian-mean theory. Part I: Nonquasigeostrophic theory for eddies on a zonal-mean flow. *J. Phys. Oceanogr.*, **35**, 165–174.
- Rhines, P., and W. Young, 1982: How rapidly is a passive scalar mixed within closed streamlines? *J. Fluid Mech.*, **133**, 133–145.
- Rogerson, A. M., P. D. Miller, L. J. Pratt, and C. K. R. T. Jones, 1999: Lagrangian motion and fluid exchange in a barotropic meandering jet. *J. Phys. Oceanogr.*, **29**, 2635–2655.
- Sallée, J. B., K. Speer, R. Morrow, and R. Lumpkin, 2008: An estimate of Lagrangian eddy statistics and diffusion in the mixed layer of the Southern Ocean. *J. Mar. Res.*, **66**, 441–463.
- Shuckburgh, E., and P. Haynes, 2003: Diagnosing transport and mixing using a tracer-based coordinate system. *Phys. Fluids*, **15**, 3342–3357.
- , H. Jones, J. Marshall, and C. Hill, 2009a: Robustness of an effective diffusivity diagnostic in oceanic flows. *J. Phys. Oceanogr.*, **39**, 1993–2009.
- , —, —, and —, 2009b: Understanding the regional variability of eddy diffusivity in the Pacific sector of the Southern Ocean. *J. Phys. Oceanogr.*, **39**, 2011–2023.
- Smith, K. S., 2007: The geography of linear baroclinic instability in the earth's oceans. *J. Mar. Res.*, **65**, 655–683.
- , and J. Marshall, 2009: Evidence for enhanced eddy mixing at middepth in the Southern Ocean. *J. Phys. Oceanogr.*, **39**, 50–69.
- Speer, K., S. Rintoul, and B. Sloyan, 2000: The diabatic deacon cell. *J. Phys. Oceanogr.*, **30**, 3212–3223.

- Stephens, C., J. Antonov, T. Boyer, M. Conkright, R. Locarini, T. O'Brien, and H. Garcia, 2001: *Temperature*. Vol. 1, *World Ocean Atlas 2001*, NOAA Atlas NESDIS X, 176 pp.
- Stone, P., 1978: Baroclinic adjustment. *J. Atmos. Sci.*, **35**, 561–571.
- Thompson, A., 2010: Jet formation and evolution in baroclinic turbulence with simple topography. *J. Phys. Oceanogr.*, **67**, in press.
- Treguier, A. M., 1999: Evaluating eddy mixing coefficients from eddy-resolving ocean models: A case study. *J. Mar. Res.*, **57**, 89–108.
- , I. Held, and V. Larichev, 1997: Parameterization of quasi-geostrophic eddies in primitive equation ocean models. *J. Phys. Oceanogr.*, **27**, 567–580.
- Visbeck, M., J. Marshall, and T. Haine, 1997: Specification of eddy transfer coefficients in coarse-resolution ocean circulation models. *J. Phys. Oceanogr.*, **27**, 381–403.
- Waugh, D. W., and E. R. Abraham, 2008: Stirring in the global surface ocean. *Geophys. Res. Lett.*, **35**, L20605, doi:10.1029/2008GL035526.
- Wunsch, C., and P. Heimbach, 2007: Practical global oceanic state estimation. *Physica D*, **230**, 197–208.
- Yuan, G.-C., L. J. Pratt, and C. K. R. T. Jones, 2002: Barrier destruction and Lagrangian predictability at depth in a meandering jet. *Dyn. Atmos. Oceans*, **35**, 41–61.
- Zurita-Gotor, P., and R. S. Lindzen, 2004a: Baroclinic equilibration and the maintenance of the momentum balance. Part I: A barotropic analog. *J. Atmos. Sci.*, **61**, 1469–1482.
- , and —, 2004b: Baroclinic equilibration and the maintenance of the momentum balance. Part II: 3D results. *J. Atmos. Sci.*, **61**, 1483–1499.